Journal of Materials Chemistry A

ROYAL SOCIETY OF CHEMISTRY

PAPER

View Article Online
View Journal | View Issue

Cite this: J. Mater. Chem. A, 2020, 8, 21833

Efficient photocatalytic CO_2 reduction mediated by transitional metal borides: metal site-dependent activity and selectivity†

Li Shi,‡[a] Pei Wang,‡[b] Qi Wang,[ac] Xiaohui Ren,[ac] Fumihiko Ichihara,[ac] Wei Zhou,[e] Hongwei Zhang,[f] Yasuo Izumi,[f] Ben Cao,[b] Shengyao Wang,[ab] Hao Chen *[b] and Jinhua Ye *[acd]

The search for novel and low-cost cocatalysts that can achieve high efficiency, while maintaining high selectivity in photocatalytic CO_2 reduction is highly desirable, yet challenging. Herein, we demonstrate that transitional metal borides (TMBs) Ni_3B, Co_3B and Fe_2B can serve as effective and low-cost cocatalysts to enhance the performance of photocatalytic CO_2 reduction under visible light, while other TMBs (TaB_2, NbB_2 and MoB) are almost ineffective. The performance of photocatalytic CO_2 reduction depends on the metal site in TMBs, among which Ni_3B exhibits the highest selectivity and activity compared to those of other TMBs. Specifically, Ni_3B exhibits a CO evolution rate of 157.7 μmol h^{-1} with selectivity of 93.0% in the presence of $[Ru(bpy)_3]Cl_2$ as a light absorber under visible light, representing state-of-the-art cocatalyst. The excellent activity of Ni_3B can be ascribed to its metallic feature that can efficiently transport photogenerated electrons from the light absorber, as well as the unique Ni–B bond that acts as an electron accumulator to provide abundant long-lived electrons to be injected into Ni^0 active sites for the activation of CO_2. These findings may provide the principle guidance for the search and design of efficient cocatalytic materials and systems for solar energy conversion.

Received 20th July 2020
Accepted 30th September 2020

DOI: 10.1039/d0ta07072f

rsc.li/materials-a

1. Introduction

The photocatalytic conversion of CO_2 to valuable chemical fuels (such as CO, CH_4 and HCOOH) with solar energy as the sole energy input has attracted intensive attention, as it not only address energy shortage but also alleviates the greenhouse effect.[1,2] Achieving highly efficient and selective photocatalytic CO_2 conversion remains a critical issue because of the high thermodynamic stability of CO_2 molecules, the limited separation efficiency of electron–hole pairs of photocatalysts, the sluggish kinetics of the multiple proton-coupled electron transfer processes, and the fierce competition of the favorable H_2 evolution reaction.[3,4] Recently, both the selectivity and activity of the photocatalytic CO_2 conversion were found to be greatly improved by cocatalysts *via* lowering the overpotential for facilitating the CO_2 reduction and assisting the separation of photogenerated charges.[5] The research of effective and low-cost cocatalysts for photocatalytic CO_2 reduction is of intense academic and industrial interest.[6] Research efforts have focused on exploring nonprecious and earth-abundant transition metals, *e.g.*, Ni, Co and Fe, and their derivative oxides, sulfide and molecular complexes as alternatives to expensive noble metal cocatalysts for improving the photocatalytic CO_2 reduction efficiency and selectivity.[7–9] However, the development of advanced cocatalysts with satisfactory activity and selectivity still face huge challenges to realize their practical applications.

For the transition metal-based cocatalysts, the metal sites are usually regarded as active sites, which tend to bond with the C and O atoms of the adsorbed CO_2 *via* strong hybridization between the 2p and 3d orbitals, followed with a successive protonation process to form hydrocarbon products.[9] During the photocatalytic reactions, the transition metal cations in cocatalytic materials would progressively reduce from high valence

[a]International Center for Materials Nanoarchitectonics (WPI-MANA), National Institute for Materials Science (NIMS), 1-1 Namiki, Tsukuba, Ibaraki, 305-0044, Japan. E-mail: Jinhua.YE@nims.go.jp

[b]College of Science, Huazhong Agricultural University, Wuhan, 430070, P. R. China. E-mail: hchenhao@mail.hzau.edu.cn

[c]Graduate School of Chemical Sciences and Engineering, Hokkaido University, Sapporo, 060-0814, Japan

[d]TU-NIMS Joint Research Center, School of Materials Science and Engineering, Tianjin University, 92 Weijin Road, Nankai District, Tianjin 300072, P. R. China

[e]Department of Applied Physics, Tianjin Key Laboratory of Low Dimensional Materials Physics and Preparing Technology, Faculty of Science, Tianjin University, Tianjin 300072, P. R. China

[f]Department of Chemistry, Graduate School of Science, Chiba University, Yayoi 1-33, Inage-ku, Chiba 263-8522, Japan

† Electronic supplementary information (ESI) available. See DOI: 10.1039/d0ta07072f

‡ These authors contributed equally to this work.

states to low valence states upon accepting electrons from photoexcited photocatalysts prior to driving the CO_2 reaction (for example, Ni^{II} to $Ni^{I/0}$, Co^{II} to $Co^{I/0}$, and Fe^{III} to $Fe^{II/I/0}$).[10–12] This reaction mechanism reveals that the lower valent transition metal cations with partially occupied 3d orbitals should be considered as more catalytically active to drive CO_2 reduction. Namely, the performance of photocatalytic CO_2 reduction can be improved by increasing the content of low oxidation transition metal species in cocatalytic materials. Nevertheless, the low oxidation transition metal species, especially involved in reactions are thermally unstable and easily oxidize to higher valency, thereby greatly limiting the development of such kind of cocatalytic materials for efficient photocatalytic CO_2 reduction.

As is known to all, the electronic states of transition metals largely depend on their coordination environment. In general, the transition metals coordinating with atoms composed by highly electronegative O, S, and N could easily lead to the highly oxidized state, which probably decreases the amount of active sites and suppresses CO_2 conversion.[5] Transitional metal borides (TMBs) raise our attention due to their fascinating properties, including good chemical stability, high thermal and electrical conductivities, as well as a variety of technological applications, such as metal–air battery, hydrogen and oxygen evolution catalyst.[13–15] TMBs comprise a diverse group of compounds, among which the Ni, Co, Fe borides have received intensive research interest because of the easy preparation, low-cost and environmentally friendly properties.[16] Previous reports have revealed that the coordination between B and transition metals would result in a partial electron transfer from B to the vacant d-orbital of the transition metals, making the transition metals electron rich and the alloying B electron-deficient.[13,14,17–19] In this case, the electron-deficient alloying B can effectively protect transition metals from oxidation, and the low oxidation transition metal active species are preserved.[13,14] Due to the existence of the low oxidation transition metal species, the utilization of TMBs as effective cocatalysts for photocatalytic CO_2 reduction is promising, but not explored yet.

Herein, we attempted to explore the cocatalytic effect of the TMBs for photocatalytic CO_2 reduction in this work. It was found that Ni_3B, Co_3B, Fe_2B were effective cocatalysts in the presence of $[Ru(bpy)_3]Cl_2$ (abbreviated as [Ru]) as light absorbers under visible light, while other TMBs (TaB_2, NbB_2 and MoB) were almost ineffective. The performance evaluation indicates the metal site-dependent activity and selectivity of the photocatalytic CO_2 reduction over TMBs, among which Ni_3B exhibits the highest CO evolution rate of 157.7 μmol h^{-1} with a selectivity of 93.0%, outperforming the state-of-the-art cocatalysts in the [Ru]-photosensitized systems. The excellent activity of Ni_3B can be ascribed to its metallic feature that can bring efficient transport of photogenerated electrons from the light absorber, as well as the unique Ni–B bonds that act as an electron accumulator to provide abundant long-lived electrons to be injected into the Ni^0 active sites for the activation of CO_2 during photocatalytic reactions.

2. Experimental section

2.1. Preparation of the metal borides

The transitional metal borides Ni_3B, Co_3B and Fe_2B nanoparticles were prepared by a simple chemical reduction and thermal annealing process. For the synthesis of Ni_3B, two separated solutions were prepared. Solution A was prepared by dissolving 0.8 g $NiCl_2 \cdot 6H_2O$ in 40 ml deionized water. Solution B was prepared by dissolving 0.4 g of $NaBH_4$ in 30 ml deionized water. After that, solution B was slowly dropped into solution A under vigorous stirring under the protection of Ar gas. The mixed solution was further stirred for 30 min. After that, the black powder was obtained by centrifugation and washing with deionized water for five times, following with drying under vacuum at 50 °C. The obtained powder was annealed under Ar at 300 °C for 2 hours. For the synthesis of Co_3B and Fe_2B, $NiCl_2 \cdot 6H_2O$ was replaced by $CoCl_2 \cdot 6H_2O$ and $FeCl_3$, and the annealing temperatures were set at 400 °C and 200 °C, respectively. TaB_2, NbB_2 and MoB powders were commercially obtained from High Purity Chemicals Corporation (Japan). Air treated Ni_3B was prepared *via* thermal annealing of Ni_3B in air at 300 °C for 2 hours. Ni nanoparticles were prepared by thermal treatment of Ni_3B in H_2 at 300 °C for 2 hours. NiO was commercially obtained from Wako Corporation (Japan).

2.2. Characterization

The XRD patterns were recorded by powder XRD on the X-ray diffractometer (X'Pert Powder, PANalytical B. V., Netherlands). The morphology of the metal borides was obtained by field emission scanning electron microscope (JSM 6701F, JEOL). TEM and HRTEM images of the samples were received from the TEM machine (FEI, Talos F200x). UV-Vis absorption spectra were obtained by Ultraviolet-visible spectroscopy (UV-2600 Shimadzu Corp., Japan). The decay time spectra were achieved on a Hamamatsu instrument (Hamamatsu C5680, Japan), and the wavelength of the excitation light was 400 nm. The chemical states of the prepared samples were recorded *via* X-ray photoelectron spectroscopy (XPS, VG-ESCA Mark II). The *in situ* Fourier-transform infrared (FTIR) spectroscopy was conducted by a JASCO FT-IR-6300h instrument in CO_2 atmosphere. The Ni K-edge X-ray absorption fine structure (XAFS) measurements were conducted at the Photon Factory Advanced Ring in Tsukuba, Japan. Ni metal foil, NiO and Ni_3B samples of analytical grade were measured. The ICP-OES data was obtained on an Agilent 7900 ICP-MS apparatus.

2.3. Photocatalytic experiments

The photocatalytic CO_2 reduction reactions were conducted in a liquid–solid reaction mode in a 100 ml quartz reactor under ambient temperature and atmospheric pressure, and the experimental setup is displayed in Fig. S2.† Typically, 5 mg metal boride cocatalysts, 30 mg $[Ru(bpy)_3]Cl_2 \cdot 6H_2O$ (commercially obtained from Sigma-Aldrich), 6 ml deionized water, 18 ml acetonitrile (MeCN) and 6 ml triethanolamine (TEOA) were mixed and sonicated in a gas-closed quartz reactor. The reaction system was evacuated completely (no O_2 or N_2 can be

detected), and then was filled with 100 kPa pure CO_2 gas. The light source was employed by a 300 W xenon arc lamp combined with a UV-cut filter (L42 filter, $\lambda > 420$ nm) and cooling water filter. The evolved H_2 and CO gas products were detected and quantified by using gas chromatographs (GC-8A, Shimadzu Co., Japan) and (GC-14B, Shimadzu Co., Japan), respectively. The carrier gas of GC was pure Ar gas. The isotope-labeled experiment was conducted using $^{13}CO_2$ instead of $^{12}CO_2$, and the generated gas was detected by the gas chromatograph-mass spectrum (GC-MS, JEOL-GCQMS, JMS-K9 and 6890N Network GC system). The cycling test of the experiment was conducted as follows. The Ni_3B powder was received by centrifugation and washing with MeCN for three times, then re-dispersed in a fresh reaction solution (30 mg $[Ru(bpy)_3]Cl_2 \cdot 6H_2O$, 6 ml water, 18 ml MeCN and 6 ml TEOA) for the next cycling experiment for a total of 5 cycles. The measurement of the apparent quantum yield (AQY) was conducted by applying a 300 W xenon arc lamp with monochromatic light band-pass filters (MIF-W, Optical Coatings Japan Co.). The radiant power energy meter (Ushio Spectroradiometer, USR-40) was applied to measure the number of incident photons. The AQY of CO evolution was calculated by the equation listed below:

$$\text{AQY}\ (\%) = \frac{\text{number of reacted electrons}}{\text{number of incident photons}} \times 100\% = \frac{\text{number of evolved CO molecules} \times 2}{\text{number of incident photons}} \times 100\%$$

3. Results and discussion

Ni, Co and Fe borides were prepared by a facile chemical reduction of metal chloride solution using $NaBH_4$ at room temperature, followed with thermal annealing procedures under Ar. X-ray diffraction (XRD) patterns (Fig. 1a–c) reveal that the as-prepared Ni, Co and Fe borides have crystalline metal borides phase structures Ni_3B (ICSD: 614985), Co_3B (ICSD: 44339) and Fe_2B (ICSD: 391328), respectively. Inductively coupled plasma optical emission spectroscopy (ICP-OES) was used to investigate the atomic ratio of Ni : B in the as-prepared Ni_3B materials, and the measured atomic ratio of Ni : B is 2.89 : 1, which is close to the stoichiometric ratio of Ni : B in Ni_3B. Fig. S1† shows the energy dispersive X-ray spectroscopy (EDX) of the as-prepared Ni_3B, and the atomic ratio of Ni : B was measured to be 4.52 : 1, revealing that Ni was the exposed site in the as-prepared Ni_3B. The morphology of the metal borides was investigated by scanning electron microscopy (SEM) images. Fig. 1d–f show that the as-prepared Ni_3B, Co_3B and Fe_2B samples present as aggregated particles, with the size in the range of tens of nanometers to hundreds of nanometers. The transition electron microscopy (TEM) image in Fig. S2† shows the typical aggregated nanoparticle shape of Ni_3B, Co_3B and Fe_2B, consistent with the SEM observation. In the high-resolution transition electron microscopy (HRTEM) images, well-resolved lattice fringe spaces of 0.235 nm, 0.205 nm and 0.201 nm are observed for Ni_3B, Co_3B and Fe_2B, corresponding to the (121), (220) and (121) crystallographic planes of the Ni_3B, Co_3B and Fe_2B phases, respectively.

The prepared Ni_3B, Co_3B and Fe_2B were then investigated as cocatalysts for photocatalytic CO_2 reduction. These studies were conducted in the reaction system with [Ru] as the light absorber and charge generator, and the system is shown in Fig. S3.† The main products of this photocatalytic system were CO and H_2, and no formation of CH_4 or formic acid was observed.[20,21] The time-dependent CO and H_2 evolution of metal borides photosensitized by [Ru] are shown in Fig. S4.† The evolution rates for

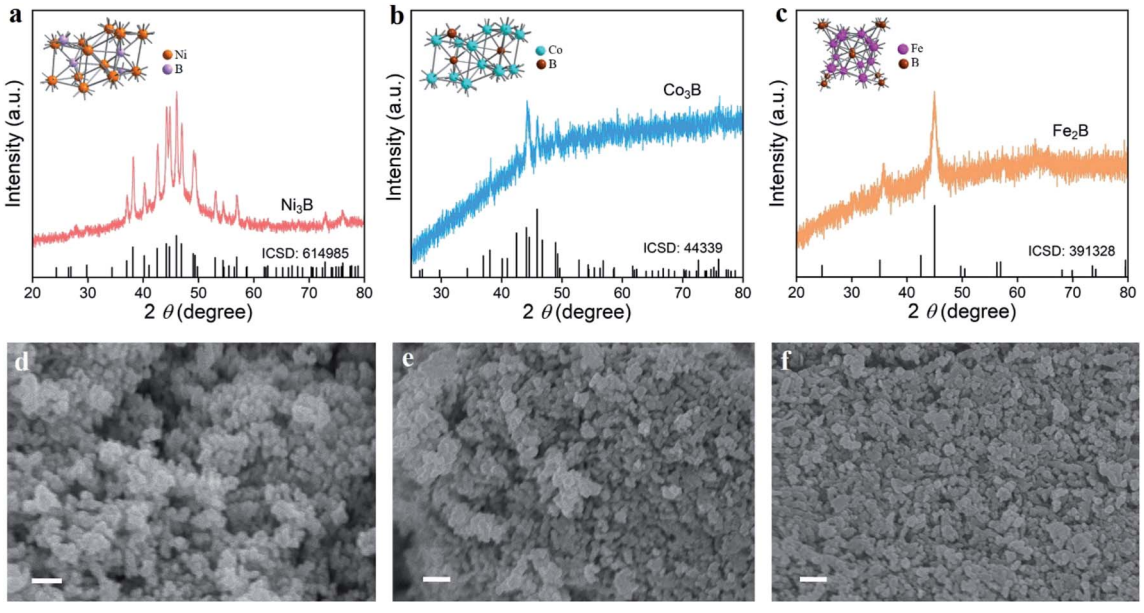

Fig. 1 XRD patterns of (a) Ni_3B, (b) Co_3B and (c) Fe_2B. The left insets in panels (a), (b), and (c) show the crystal structures of Ni_3B, Co_3B and Fe_2B, respectively. SEM images of (d) Ni_3B, (e) Co_3B, and (f) Fe_2B. Scale bar: (d) 200 nm, (e) 400 nm, (f) 400 nm.

CO and H_2 decrease after 1 hour continuous testing (Fig. S4†). This stagnation effect is mainly due to the photobleaching of the [Ru] light absorber that has been commonly reported in previous works.[20,21] Fig. 2a summarizes the photocatalytic performances of metal boride cocatalysts in the initial one hour. Ni_3B/[Ru] (Ni_3B as the cocatalyst and [Ru] as the light absorber) exhibits a considerable CO evolution rate of 157.7 μmol h^{-1} with a H_2 production rate of 11.8 μmol h^{-1} during the 1 h reaction period, obtaining a high CO selectivity of 93.0%. The apparent quantum yield (AQY) of the CO evolution along with the wavelength of the incident light was investigated. As shown in Fig. 2b, the variation tendency of AQY matches well with the light absorption spectrum of [Ru], indicating the CO_2 reduction reaction occurs photocatalytically by the [Ru] light absorber. Notably, an AQY at the monochromatic light of 420 nm was measured as high as 4.5%. The achieved photocatalytic CO_2 reduction performance outperforms the state-of-the-art cocatalysts under comparable conditions in the literature, as shown in Table S1.†[20–27] Without metal borides in the photocatalytic system, [Ru] only exhibits the CO evolution rate of 2.9 μmol h^{-1} together with CO selectivity of 37.7%. The CO and H_2 evolutions are completely terminated in the absence of [Ru]. These results indicate the cocatalytic effect of metal borides in the photocatalytic CO_2 reduction reaction. Co_3B and Fe_2B can also act as the cocatalysts for photocatalytic CO_2 reduction. However, their CO evolution rates and selectivities are much lower than those of Ni_3B (Fig. 2a).

Given that Ni_3B achieves high activity, its stability was then evaluated. The used Ni_3B catalyst was collected and re-dispersed in a fresh reaction solution with newly added [Ru] for stability tests. As presented in Fig. 2c, the used Ni_3B cocatalyst retained ~94% of its original performance after five cycle tests, demonstrating its high stability for photocatalytic CO_2 reduction. The SEM image and XRD pattern of Ni_3B after photocatalytic reaction further confirm the high stability (Fig. S5 and S6†). The evolution of CO was not observed under either Ar or without light, indicating that the CO product indeed originated from the photocatalytic conversion of CO_2 molecules (Fig. S7†). To further certify the carbon source of the produced CO, ^{13}C-labelled isotopic experiment using $^{13}CO_2$ was conducted in the Ni_3B/[Ru] system, and the product was then analyzed by GC-MS machine. The CO product appeared at the GC peak of 6.06 min, and the other two peaks in the GC spectrum are O_2 and N_2, respectively, derived from the air of the sampling needle (Fig. 2d). The analysis of CO revealed a value of $m/z = 29$, corresponding to ^{13}CO. This result clearly demonstrates that the generated CO indeed comes from the reduction of CO_2.

The above results demonstrate that the Ni, Co and Fe borides act as efficient cocatalysts for the photoreduction of CO_2. It is very interesting to investigate the cocatalytic effect of other

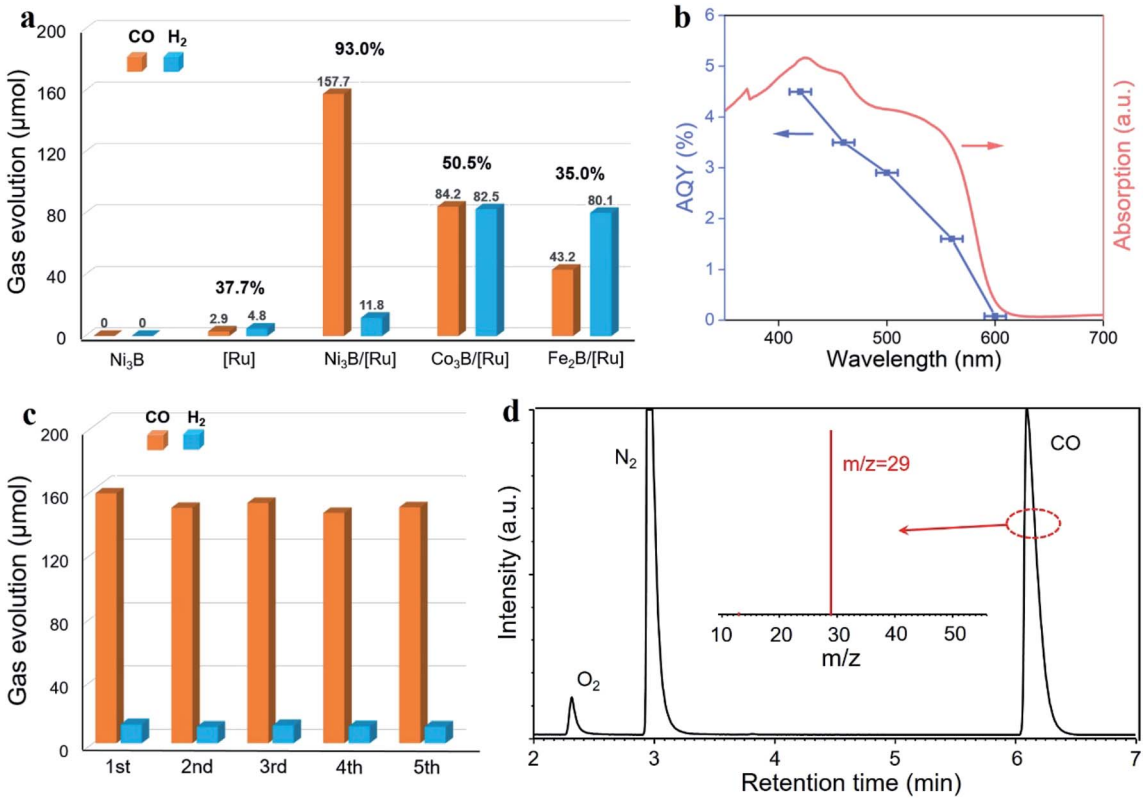

Fig. 2 (a) Photocatalytic CO_2 reduction activities over different catalysts in one hour. The percentage of each catalyst represents the selectivity of CO. (b) Wavelength dependence of the AQY over Ni_3B/[Ru], and the UV-Vis absorption spectrum of the [Ru] light absorber. (c) Cycling stability test over Ni_3B/[Ru]. Each test was conducted for one hour. (d) Gas chromatography-mass spectra (GC-MS) of ^{13}CO generated in the photocatalytic reduction of $^{13}CO_2$ over Ni_3B/[Ru].

metal borides. TaB_2, NbB_2 and MoB were selected as they also have stable structures. The photocatalytic performances of the TaB_2, NbB_2 and MoB cocatalysts in the presence of [Ru] in the initial hour are shown in Fig. S8.† It clearly indicates that TaB_2, NbB_2 and MoB were not effective cocatalysts for CO_2 photoreduction, since the CO evolution rates were not improved. These results indicate that the cocatalytic performance is dependent on the metal sites of the metal borides. The high cocatalytic activities of the Ni, Co and Fe borides can be attributed to the intrinsic catalytic properties of the Ni, Co and Fe active sites for CO_2 activation.[28,29]

Generally speaking, the photocatalytic conversion of CO_2 to CO undergoes the formation of a formate intermediate (COOH*) *via* $CO_2^* + H^+ + e^- \rightarrow COOH^*$.[22] To investigate the CO_2 photoreduction process on the Ni_3B/[Ru] system, an *in situ* Fourier-transform infrared spectroscopy (FTIR) investigation was conducted. As shown in Fig. 3a, a strong broad absorption peak centered at 2329 cm^{-1} appears during CO_2 photoreduction, which is ascribed to the absorbed CO_2 molecule.[30] In addition, the broad absorption peaks centered at 1522 cm^{-1} and 1354 cm^{-1} are assigned to the carbonate-type species and the adsorbed formate (COOH*) species, respectively.[30] Furthermore, the broad absorption peaks in the range of 1670–1820 cm^{-1} with a center located at 1731 cm^{-1} correspond to the asymmetric stretching of O–C=O, which also belong to the intermediate formate (COOH*) species.[31] It can be seen that with the increase of the irradiation time, the intensities of these peaks gradually increase, illustrating the formation of the formate intermediate during the CO_2 photoreduction process. CO* is then produced from the COOH* conversion by a proton–electron transfer reduction process ($COOH^* + H^+ + e^- \rightarrow CO^* + H_2O$), and CO is finally released from the dissociation of the absorbed CO* adduct ($CO^* \rightarrow CO$).[22] The cocatalytic performances of the metal borides follow the order: Ni_3B > Co_3B > Fe_2B. In order to investigate the origin of the metal-site-dependent performance of the metal borides for CO_2 photoreduction, density functional theory (DFT) calculations were then conducted (see Computational details in ESI†). The optimized bulk Ni_3B, Co_3B, and Fe_2B lattice parameters were in good agreement with the experimental value, as shown in Table S2.† The (010) surface was chosen for simulation, as the Ni_3B (010) surface had the lowest barrier of 0.49 eV. The corresponding surface energy and structure of the intermediate along the reaction path are shown in Fig. S9 and S10,† respectively. The reaction free energy diagrams of the CO_2 reduction over Ni_3B, Co_3B and Fe_2B are plotted in Fig. 3b. As for Ni_3B, Co_3B and Fe_2B, their rate-determining steps of the reaction are the dissociation of CO* adduct, which are 0.49 eV, 0.81 eV and 1.33 eV, respectively. The free energy barrier of the CO_2 reduction shows the expected trend of Ni_3B < Co_3B < Fe_2B, consistent with the experimental results that Ni_3B shows higher CO_2 reduction activity than Co_3B and Fe_2B.

The above results have revealed the highly active Ni_3B for promoting the photocatalytic CO_2 reduction reaction, and now we are in a position to disclose the advantages of this structure. Noting that the electronic structure and chemical state of cocatalysts play significant roles in inferring their photocatalytic CO_2 reduction performances, X-ray photoelectron spectroscopy (XPS) was utilized to reveal the chemical states of Ni_3B. Fig. 4a shows the high-resolution XPS spectrum of Ni 2p of Ni_3B. The peak located at the binding energy of 852.2 eV can be attributed to Ni^0, originating from the Ni–B bond.[32] Notably, the coordination between B and the transition metals would result in a partial electron transfer from B to the vacant d-orbital of the transition metals. This would make the transition metals electron-rich and the alloying B electron-deficient. Thus, the low oxidation transition metals are formed.[13] A weak peak at a higher binding energy of 855.8 eV corresponds to the Ni^{2+} signal, resulting from the inevitable surface oxidation in air storage.[33] The XPS spectrum of B 1s of Ni_3B is displayed in Fig. S11,† and the peaks located at 191.9 eV and 187.7 eV correspond to B–O bonding and B–Ni bonding, respectively.[32] The formation of B–O bonding is derived from the surface oxidation in air. To probe the chemical environment of the Ni element in Ni_3B, the Ni K-edge extended X-ray absorption fine structure (EXAFS) and X-ray absorption near-edge structure (XANES) spectroscopies were measured. Fig. 4b shows the normalized XANES spectra collected at the Ni K-edge for the Ni metal, NiO and Ni_3B. The pre-edge region of Ni_3B consists of a small peak at ~8334 eV, whose shape and position are similar

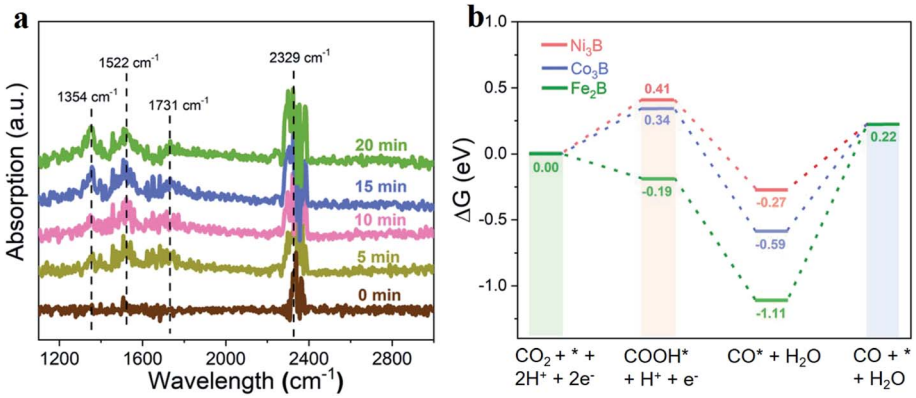

Fig. 3 (a) *In situ* FTIR spectra of photocatalytic CO_2 reduction under visible light over [Ru]-photosensitized Ni_3B. (b) Reaction free energy diagrams of the CO_2 reduction over Ni_3B, Co_3B and Fe_2B.

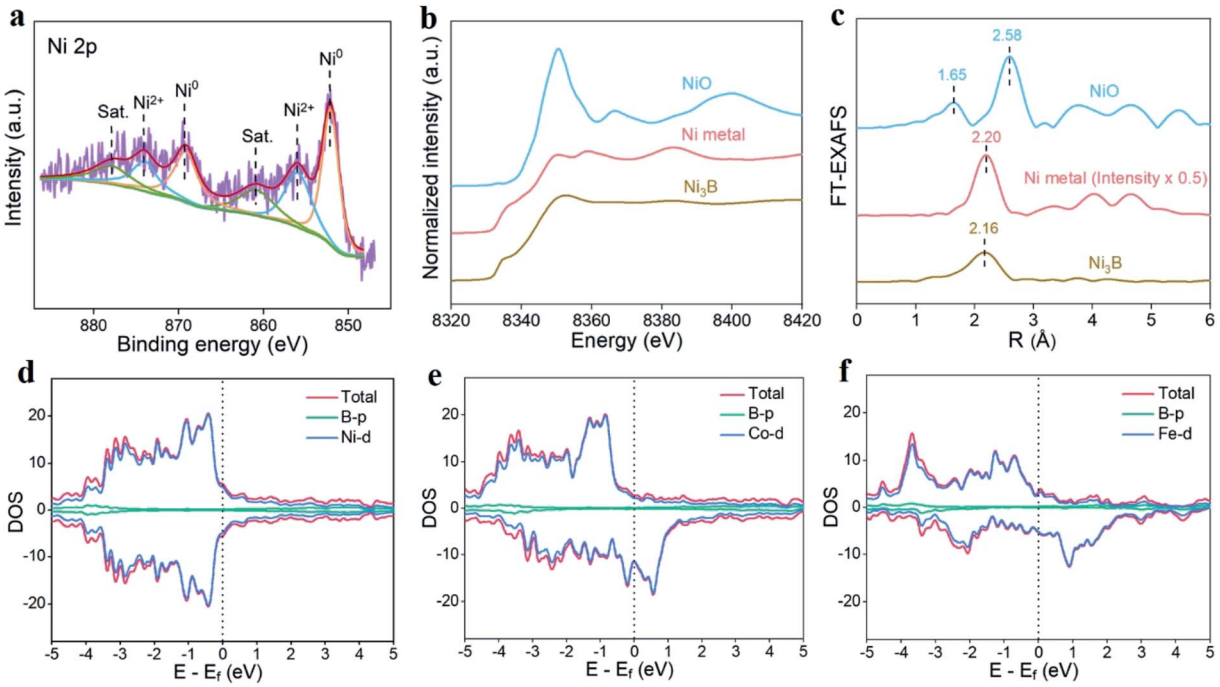

Fig. 4 (a) Ni 2p XPS spectrum of Ni_3B. (b) Ni K-edge XANES spectra and (c) the Fourier transform of angular wave number $(k)^3$-weighted EXAFS spectra for the Ni metal, NiO and Ni_3B. (d–f) Calculated DOS of Ni_3B, Co_3B and Fe_2B, respectively.

to those of the Ni metal, indicating predominance of the Ni^0 state in the sample. Fig. 4c shows the Fourier-transformed EXAFS spectra of the Ni metal, NiO and Ni_3B. For the Ni metal, the peak at 2.20 Å corresponds to the Ni–Ni bond. Ni_3B exhibits a much weaker peak centered at 2.16 Å, which is attributed to the Ni–Ni scattering pair in Ni_3B.[34,35] This peak position is smaller than that of Ni–Ni (2.20 Å) in the Ni foil standard sample, which results from the chemical interaction involving the hybridization and electron transfer between the B 2p states with the Ni metal d orbitals.[34,35] The Ni–O bond at 1.65 Å and Ni–O–Ni bond at 2.58 Å are absent in Ni_3B, indicating that the portion of surface Ni^{2+} oxidation species in Ni_3B is very low. Ni_3B displays a metallic feature, which can be confirmed by DFT calculations. As shown in Fig. 4d, the total density of states (DOS) of Ni_3B are mainly ascribed to the contribution from the d orbitals of the Ni atom, and the values of DOS of Ni_3B around the Fermi level (E_f) are all continuous without an obvious bandgap, demonstrating the metallic feature of Ni_3B. In addition, the p orbitals of B also displays the continuous nature, indicating the covalent interaction between B and Ni in the metallic state.[36] Similarly, Co^0 and Fe^0 also exist in Co_3B and Fe_2B, respectively, which can be confirmed by their XPS spectra (Fig. S12†), consistent with previous reports.[37,38] The metallic features of Co_3B and Fe_2B are also confirmed by their calculated DOS distributions (Fig. 4e and f). The metallic character of the Ni_3B, Co_3B and Fe_2B materials could bring an efficient transport of charge carriers. Thus, they can act as highly active cocatalysts to promote photocatalytic performances.

Fig. 5a shows the valence band XPS (VB-XPS) spectrum of Ni_3B. It can be seen that the E_f of Ni_3B is occupied by continuous electronic occupied states, further disclosing its metallic feature. Fig. 5b shows the calculated charge distribution of Ni_3B, which indicates that charges are accumulated on the Ni–B bond. This unique feature enables the Ni–B bond acting as an electron accumulator to store electrons, which can provide abundant long-lived electrons to be injected into the Ni^0 active sites for the activation of CO_2 during photocatalytic reactions. Time-resolved PL decay spectroscopy was then utilized to experimentally reveal the dynamic charge behavior of the photocatalytic system.[39] Fig. 5c shows the decay curves of [Ru] with and without Ni_3B. The fitted average lifetimes are shown in Table S3,† which indicates that the PL average lifetime increases in the following order: pure [Ru] < Ni_3B/[Ru]. The lengthened lifetime of [Ru] in the presence of Ni_3B is ascribed to the electron transfer from [Ru] to Ni_3B, and the electrons are accumulated on Ni_3B. The mechanism for the photocatalytic CO_2 reduction is displayed in Fig. 5d and S13† based on above results, and the previous reports in the Ru-photosensitized systems.[22] Under visible light irradiation, the electrons generated from the photosensitizer [Ru] can be transferred to the metal boride cocatalysts. Then, the CO_2 molecules absorbed on the surface of the metal borides are reduced to CO. The H_2 evolution is regarded as a competing reaction to the CO evolution, and Ni boride is demonstrated as the most effective cocatalyst to suppress the H_2 evolution and simultaneously maintain a record high CO evolution rate.

To demonstrate the dominant role of the Ni–B bond in Ni_3B for the photocatalytic CO_2 reduction, the cocatalytic performances of Ni_3B, air-treated Ni_3B, Ni nanoparticles and NiO were evaluated and compared. Air-treated Ni_3B was prepared by

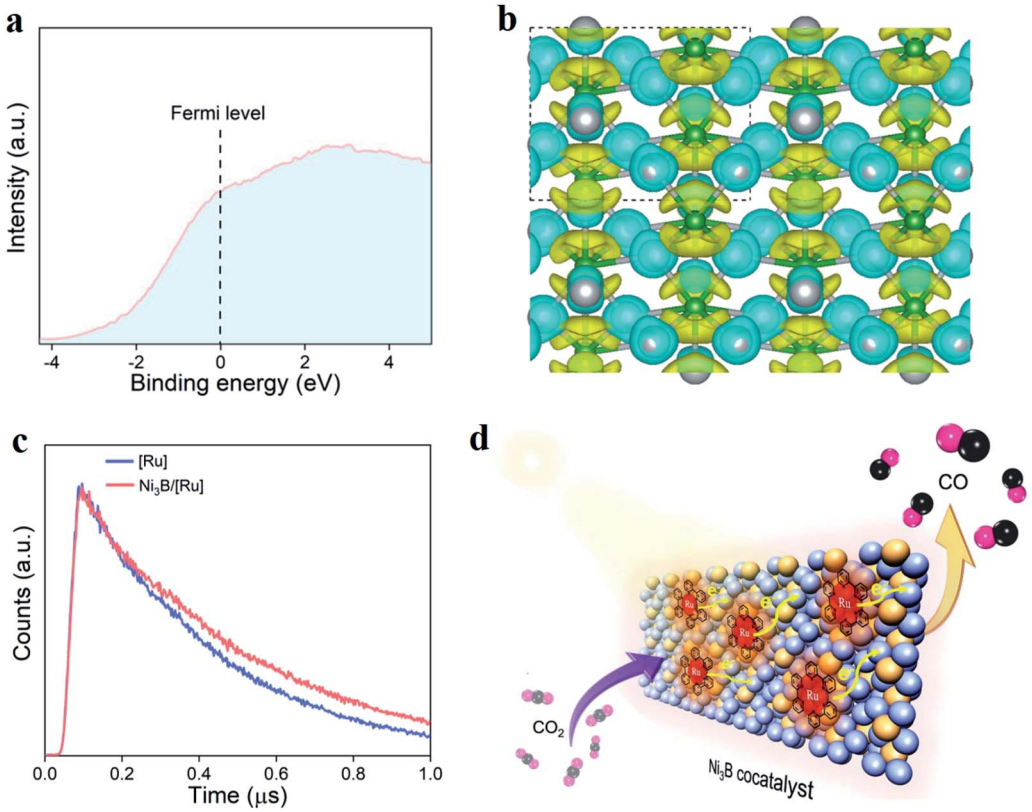

Fig. 5 (a) VB-XPS spectrum of Ni_3B. (b) Charge density distribution of Ni_3B. The green ball is B and the grey ball is Ni, and the value of the isosurface is 0.01 e $Å^{-3}$. (c) Time-resolved PL decay spectra of [Ru] with and without Ni_3B. (d) Proposed mechanism for the photocatalytic reduction of CO_2 to CO over [Ru]-photosensitized Ni_3B under visible light irradiation.

thermal treatment of Ni_3B in air at 300 °C for 2 hours, and Ni nanoparticles were prepared by thermal treatment of Ni_3B in H_2 at 300 °C for 2 hours. The XRD pattern indicates that the air-treated Ni_3B also displays a crystalline Ni_3B phase structure (Fig. S14†), and the H_2-treated Ni_3B displays a crystalline Ni phase structure (Fig. S15†). The SEM images show that the air-treated Ni_3B and H_2-treated Ni_3B exhibit aggregated particles, which have similar morphology compared with Ni_3B (Fig. S16†). However, the content of the Ni–B bond on the surface of the air-treated Ni_3B is significantly decreased, as revealed by XPS spectra (Fig. S17†). The decreased content of the Ni–B bond is caused by the thermal oxidation of Ni^0 to Ni^{2+} in air. The photocatalytic performances of Ni_3B, air-treated Ni_3B, Ni nanoparticles and NiO in the presence of [Ru] are shown in Fig. S18.† It is obvious that Ni_3B exhibits much higher activity and selectivity than air-treated Ni_3B, Ni nanoparticles and NiO, demonstrating the dominant role of the Ni–B bond for promoting the photocatalytic CO_2 activation and reduction. The lower photocatalytic performance of NiO is due to its semiconducting features, whose conductivity and electron transfer efficiency are much lower than that of Ni_3B (Fig. S19†). The existence of the Ni–B bond in Ni_3B is beneficial for the desorption of the CO molecule, which can be revealed by the DFT calculations. The calculated CO adsorption energy was −0.27 eV over the Ni_3B (010) surface, which is much weaker than that over Ni (111) (−0.41 eV and −0.72 eV on the top site and hollow site, respectively) (see computational details). The charge density analysis in Fig. S20† further verifies the lower adsorption energy of CO over the Ni_3B (010) surface compared to that over the Ni (111) surface, indicating that the CO product is much easier to release from the Ni_3B surface, which is one of the reasons why Ni_3B exhibits much higher activity than Ni nanoparticles for photocatalytic CO_2 reduction (Fig. S18†).

4. Conclusion

In summary, we have demonstrated that the TMBs Ni_3B, Co_3B, Fe_2B are effective cocatalysts for photocatalytic CO_2 reduction under visible light, while other TMBs (TaB_2, NbB_2 and MoB) are almost ineffective. Experimental results reveal that the cocatalytic CO_2 reduction performances of TMBs exhibit metal site-dependent activity and selectivity, among which Ni_3B is demonstrated as the most effective cocatalyst, obtaining both highest CO evolution rate and highest selectivity compared to other TMBs. Specifically, a record high CO evolution rate of 157.7 μmol h^{-1} with selectivity of 93.0% was obtained over the Ni_3B cocatalyst. The mechanism investigation indicates that the excellent activity of the Ni_3B cocatalyst can be ascribed to its metallic feature, which can bring an efficient transport of photogenerated electrons from the light absorber, as well as the unique Ni–B bond that acts as an electron accumulator to provide abundant long-lived electrons to be injected into the Ni^0

active sites for the activation of CO_2 during photocatalytic reactions. This work may provide fundamental guidance for the design of efficient cocatalytic materials and systems for solar water splitting, CO_2 reduction and many other energy conversion reactions.

Author contributions

L. Shi and P. Wang contributed equally to this work. L. Shi and J. Ye conceived and designed the experiments. L. Shi fabricated the materials. P. Wang, Q. Wang and W. Zhou completed the theoretical computations and discussed the theoretical results. L. Shi and X. Ren designed the experimental devices and performed the photocatalytic experiments. F. Ichihara conducted the time-resolved PL decay measurement. H. Zhang and Y. Izumi performed the EXAFS and XANES measurements and analyzed the data. B. Cao and S. Wang conducted the TEM measurements and analyzed the data. L. Shi, P. Wang and S. Wang wrote the manuscript. J. Ye and H. Chen supervised the research work and revised the manuscript. All authors contributed to the general discussion.

Conflicts of interest

The authors declare no competing financial interests.

Acknowledgements

This work received financial support from the World Premier International Research Center Initiative (WPI Initiative) on Materials Nanoarchitectonics (MANA), MEXT (Japan), JSPS KAKENHI (JP18H02065), the Photo-excitonix Project at Hokkaido University, National Natural Science Foundation of China (No. 21633004, No. 52073110, and No. 2190020614), and the Fundamental Research Funds for the Central Universities (No. NE2019103 and No. 2662018QD041).

References

1 W. Tu, Y. Zhou and Z. Zou, *Adv. Mater.*, 2014, **26**, 4607–4626.
2 L. Shi, T. Wang, H. Zhang, K. Chang and J. Ye, *Adv. Funct. Mater.*, 2015, **25**, 5360–5367.
3 X. Liu, S. Inagaki and J. Gong, *Angew. Chem., Int. Ed.*, 2016, **55**, 14924–14950.
4 X. Meng, Q. Yu, G. Liu, L. Shi, G. Zhao, H. Liu, P. Li, K. Chang, T. Kako and J. Ye, *Nano Energy*, 2017, **34**, 524–532.
5 J. Ran, M. Jaroniec and S. Z. Qiao, *Adv. Mater.*, 2018, **30**, 1704649.
6 G. Zhao, X. Huang, X. Wang and X. Wang, *J. Mater. Chem. A*, 2017, **5**, 21625–21649.
7 S. Nahar, M. F. M. Zain, A. A. H. Kadhum, H. A. Hasan and M. R. Hasan, *Materials*, 2017, **10**, 629.
8 B. Ma, G. Chen, C. Fave, L. Chen, R. Kuriki, K. Maeda, O. Ishitani, T. C. Lau, J. Bonin and M. Robert, *J. Am. Chem. Soc.*, 2020, **13**, 6188–6195.
9 X. Li, J. Yu, M. Jaroniec and X. Chen, *Chem. Rev.*, 2019, **119**, 3962–4179.
10 M. Khalil, J. Gunlazuardi, T. A. Ivandini and A. Umar, *Renewable Sustainable Energy Rev.*, 2019, **113**, 109246.
11 Z. Guo, S. Cheng, C. Cometto, E. Anxolabehere-Mallart, S. M. Ng, C. C. Ko, G. Liu, L. Chen, M. Robert and T. C. Lau, *J. Am. Chem. Soc.*, 2016, **138**, 9413–9416.
12 H. Rao, L. C. Schmidt, J. Bonin and M. Robert, *Nature*, 2017, **548**, 74–77.
13 H. Sun, J. Meng, L. Jiao, F. Cheng and J. Chen, *Inorg. Chem. Front.*, 2018, **5**, 760–772.
14 S. Carenco, D. Portehault, C. Boissiere, N. Mezailles and C. Sanchez, *Chem. Rev.*, 2013, **113**, 7981–8065.
15 S. Gupta, M. K. Patel, A. Miotello and N. Patel, *Adv. Funct. Mater.*, 2019, **30**, 1906481.
16 G. Akopov, M. T. Yeung and R. B. Kaner, *Adv. Mater.*, 2017, **29**, 1604506.
17 R. Fernandes, A. Chunduri, S. Gupta, R. Kadrekar, A. Arya, A. Miotello and N. Patel, *Electrochim. Acta*, 2020, **354**, 136738.
18 S. Gupta, N. Patel, A. Miotello and D. C. Kothari, *J. Power Sources*, 2015, **279**, 620–625.
19 N. Patel, G. Guella, A. Kale, A. Miotello, B. Patton, C. Zanchetta, L. Mirenghi and P. Rotolo, *Appl. Catal., A*, 2007, **323**, 18–24.
20 S. Wang, B. Y. Guan and X. W. Lou, *Energy Environ. Sci.*, 2018, **11**, 306–310.
21 C. Gao, S. Chen, Y. Wang, J. Wang, X. Zheng, J. Zhu, L. Song, W. Zhang and Y. Xiong, *Adv. Mater.*, 2018, **30**, 1704624.
22 B. Han, X. Ou, Z. Deng, Y. Song, C. Tian, H. Deng, Y. J. Xu and Z. Lin, *Angew. Chem., Int. Ed.*, 2018, **57**, 16811–16815.
23 S. Wang, W. Yao, J. Lin, Z. Ding and X. Wang, *Angew. Chem., Int. Ed.*, 2014, **53**, 1034–1038.
24 C. Gao, Q. Meng, K. Zhao, H. Yin, D. Wang, J. Guo, S. Zhao, L. Chang, M. He, Q. Li, H. Zhao, X. Huang, Y. Gao and Z. Tang, *Adv. Mater.*, 2016, **28**, 6485–6490.
25 J. Qin, S. Wang and X. Wang, *Appl. Catal., B*, 2017, **209**, 476–482.
26 Y. Gao, L. Ye, S. Cao, H. Chen, Y. Yao, J. Jiang and L. Sun, *ACS Sustainable Chem. Eng.*, 2017, **6**, 781–786.
27 S. Wang, Y. Hou and X. Wang, *ACS Appl. Mater. Interfaces*, 2015, **7**, 4327–4335.
28 J. Wu, Y. Huang, W. Ye and Y. Li, *Adv. Sci.*, 2017, **4**, 1700194.
29 L. Chen, Z. Guo, X. G. Wei, C. Gallenkamp, J. Bonin, E. Anxolabehere-Mallart, K. C. Lau, T. C. Lau and M. Robert, *J. Am. Chem. Soc.*, 2015, **137**, 10918–10921.
30 Y. Liu, S. Chen, X. Quan and H. Yu, *J. Am. Chem. Soc.*, 2015, **137**, 11631–11636.
31 A. Li, Q. Cao, G. Zhou, B. Schmidt, W. Zhu, X. Yuan, H. Huo, J. Gong and M. Antonietti, *Angew. Chem., Int. Ed.*, 2019, **58**, 14549–14555.
32 W. J. Jiang, S. Niu, T. Tang, Q. H. Zhang, X. Z. Liu, Y. Zhang, Y. Y. Chen, J. H. Li, L. Gu, L. J. Wan and J. S. Hu, *Angew. Chem., Int. Ed.*, 2017, **56**, 6572–6577.
33 X. Chen, Z. Yu, L. Wei, Z. Zhou, S. Zhai, J. Chen, Y. Wang, Q. Huang, H. E. Karahan, X. Liao and Y. Chen, *J. Mater. Chem. A*, 2019, **7**, 764–774.
34 I. Saldan, S. Hino, T. D. Humphries, O. Zavorotynska, M. Chong, C. M. Jensen, S. Deledda and B. C. Hauback, *J. Phys. Chem. C*, 2014, **118**, 23376–23384.

35 J. Masa, I. Sinev, H. Mistry, E. Ventosa, M. Mata, J. Arbiol, M. Muhler, B. R. Cuenya and W. Schuhmann, *Adv. Energy Mater.*, 2017, **7**, 1700381.
36 J. Jiang, M. Wang, W. Yan, X. Liu, J. Liu, J. Yang and L. Sun, *Nano Energy*, 2017, **38**, 175–184.
37 Z. Chen, Q. Kang, G. Cao, N. Xu, H. Dai and P. Wang, *Int. J. Hydrogen Energy*, 2018, **43**, 6076–6087.
38 H. Li, P. Wen, Q. Li, C. Dun, J. Xing, C. Lu, S. Adhikari, L. Jiang, D. L. Carroll and S. M. Geyer, *Adv. Energy Mater.*, 2017, **7**, 1700513.
39 L. Shi, L. Yang, W. Zhou, Y. Liu, L. Yin, X. Hai, H. Song and J. Ye, *Small*, 2018, **14**, 1703142.